Comput. Methods Appl. Mech. Engrg. 200 (2011) 2903–2915

Contents lists available at ScienceDirect

Comput. Methods Appl. Mech. Engrg.

journal homepage: www.elsevier.com/locate/cma

Computational competition of symmetric mixed FEM in linear elasticity ☆,☆☆

C. Carstensen [a,b,*], M. Eigel [a], J. Gedicke [a]

[a] Institut für Mathematik, Humboldt-Universität zu Berlin, Unter den Linden 6, 10099 Berlin, Germany
[b] Department of Computational Science and Engineering, Yonsei University, 120-749 Seoul, Republic of Korea

ARTICLE INFO

Article history:
Received 15 October 2010
Received in revised form 4 February 2011
Accepted 24 May 2011
Available online 6 June 2011

Keywords:
Finite element method
Non-conforming
Symmetric mixed
Locking
Computational survey
Linear elasticity

ABSTRACT

The Navier–Lamé equation for linear elasticity has evoked the design of various non-standard finite element methods (FEM) in order to overcome the locking phenomenon. Recent developments of Arnold and Winther in 2002 involve a stable mixed method which strongly fulfils the symmetry constraint. Subsequently, two $H(\mathrm{div})$ non-conforming symmetric mixed methods arose. This paper comments on the implementation of all those mixed FEM and provides a numerical comparison of the different symmetric mixed schemes for linear elasticity. The computational survey also includes the low-order elements of weak symmetry (PEERS), the non-conforming Kouhia and Stenberg (KS) elements plus the conforming displacement P_k-FEM for $k = 1, 2, 3, 4$. Numerical experiments confirm the theoretical convergence rates for sufficiently smooth solutions and illustrate the superiority of the symmetric MFEM amongst the methods of second or third order.

1. Introduction

The numerical solution of the Navier–Lamé equation with mixed weak formulations allows a robust approximation even if the crucial Lamé parameter passes to the incompressible limit when the Poisson ratio approaches 1/2, see [8, Chapter IV Section 3]. In low-order displacement formulations, the well-known locking effect causes *a priori* error estimates to deteriorate. While there are many known stable mixed finite element methods (MFEM), the additional symmetry constraint implied for the stress tensor proved to be difficult to impose in numerical schemes. This has resulted in the introduction of discretisations with no or reduced symmetry incorporated in the discrete stress space [2,19,11]. The first MFEM which were designed especially to fulfil the stress symmetry without the need of a sub-grid are due to Arnold and Winther [1, 4, 5, 6, 7]. As discussed in [7], the continuity property imposed on the stress field in the conforming MFEM substantially increases complexity of the finite elements. Since (complete) continuity is not required in the mixed formulation of linear elasticity, non-conforming MFEM can be an efficient and easier to implement alternative to conforming elements. Table 1 displays the MFEM compared in this paper. While the conforming lowest-order MFEM of Arnold and Winther AW30 and AW24 have 30 and 24 degrees of freedom and are based on a polynomial basis of degree 3, the non-conforming AW21 and AW15 MFEM are based on a quadratic polynomial basis with 21 and 15 degrees of freedom, as depicted in the first row of Table 1. The recently introduced S15 and S27 MFEM due to Schöberl and Sinwel [18] are based on linear and quadratic polynomials and have 15 and 27 degrees of freedom.

This paper is devoted to the computational competition of several FEM displayed in Table 2 for the Navier–Lamé equation of linear elasticity. Our interest hereby lies on the numerical examination of the rather novel MFEM of Arnold and Winther [5,7,13] and the elements introduced by Schöberl and Sinwel [18]. For some of these elements we discuss the implementation topics that have not been presented yet. Of particular interest is the numerical competition of the many newly available mixed finite elements of order one up to three with traditional displacement-oriented FEM of the same orders. Since P_4 is locking free [9] in contrast to P_k, $k = 1, 2, 3$, it is included in the survey as well as the low-order MFEM of weak symmetry [2] (PEERS) and the non-conforming KS-FEM [17]. We note that there are some recent elements which we could not include in this survey such as [14,15]. Moreover, while there are several MFEM with weak symmetry constraints that might also have been worth to consider in our comparison,

☆ Supported by the DFG Research Center MATHEON "Mathematics for key technologies", the World Class University (WCU) program through the National Research Foundation of Korea (NRF) funded by the Ministry of Education, Science and Technology R31-2008-000-10049-0, and the graduate school BMS "Berlin Mathematical School" in Berlin.

☆☆ Dedicated to Professor Erwin Stein on the occasion of his 80th birthday.

* Corresponding author at: Institut für Mathematik, Humboldt-Universität zu Berlin, Unter den Linden 6, 10099 Berlin, Germany.
E-mail addresses: cc@mathematik.hu-berlin.de (C. Carstensen), eigel@mathematik.hu-berlin.de (M. Eigel), gedicke@mathematik.hu-berlin.de (J. Gedicke).

0045-7825/$ - see front matter © 2011 Elsevier B.V. All rights reserved.
doi:10.1016/j.cma.2011.05.013

Table 1
Symmetric mixed finite elements schemes.

Name	Finite element schemes	Function spaces	Continuity constraints
AW21 (15 + 6 dofs)	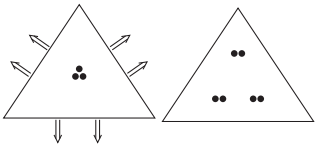	$\Sigma_T := \{\sigma \in P_2(T;\mathbb{S}) \mid v_E \cdot (\sigma v_E) \in P_1(E) \forall E \in \partial T\}$ $\mathcal{V}_T := P_1(T;\mathbb{R}^2)$	$\forall E \in \partial T,\ v \in P_1(E;\mathbb{R}^2)$ $\int_E (\sigma v_E) \cdot v\, ds$
AW15 (12 + 3 dofs)	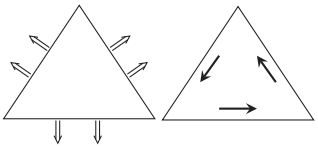	$\Sigma_T := \{\sigma \in P_2(T;\mathbb{S}) \mid \mathrm{div}\sigma \in \mathrm{RM}(T), v_E \cdot (\sigma v_E) \in P_1(E) \forall E \in \partial T\}$ $\mathcal{V}_T := \mathrm{RM}(T)$	$\forall E \in \partial T,\ v \in P_1(E;\mathbb{R}^2)$ $\int_E (\sigma v_E) \cdot v\, ds$
AW30 (24 + 6 dofs)	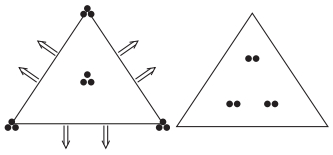	$\Sigma_T := \{\sigma \in P_3(T,\mathbb{S}) \cap H(\mathrm{div},\Omega;\mathbb{S}) \mid \mathrm{div}\sigma \in P_1(T;\mathbb{R}^2)\}$ $\mathcal{V}_T := P_1(T;\mathbb{R}^2)$	σv
AW24 (21 + 3 dofs)	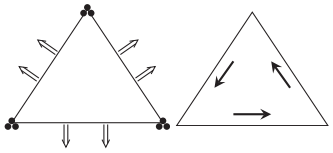	$\Sigma_T := \{\sigma \in P_3(T;\mathbb{S}) \cap H(\mathrm{div},\Omega;\mathbb{S}) \mid \mathrm{div}\sigma \in \mathrm{RM}(T)\}$ $\mathcal{V}_T := \mathrm{RM}(T)$	σv
S15 (9 + 6 dofs)	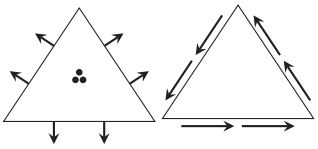	$\Sigma_T := \{\sigma \in P_1(T;\mathbb{S}) \cap H(\mathrm{div}\,\mathrm{div},\Omega;\mathbb{S})\}$ $\mathcal{V}_T := \{v \in P_1(T;\mathbb{R}^2) \cap H(\mathrm{curl},\Omega;\mathbb{R}^2)\}$	$\forall E \in \partial T$ $v_E \cdot (\sigma v_E)$ $v \cdot \tau_E$
S27 (15+12 dofs)	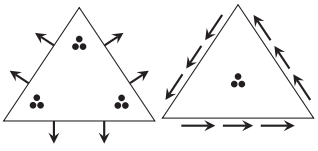	$\Sigma_T := \{\sigma \in P_2(T;\mathbb{S}) \cap H(\mathrm{div}\,\mathrm{div},\Omega;\mathbb{S})\}$ $\mathcal{V}_T := \{v \in P_2(T;\mathbb{R}^2) \cap H(\mathrm{curl},\Omega;\mathbb{R}^2)\}$	$\forall E \in \partial T$ $v_E \cdot (\sigma v_E) \in P_1(E)$ $v \cdot \tau_E$

see e.g. [3,16,12], our focus lies on symmetric methods. The reason for including PEERS and KS-FEM is the great popularity of these methods in the engineering community. We also mention that, although out of the scope of this paper, higher-order PEERS are available which probably would show a more favourable performance than the lowest-order version used in the examples.

While robustness, locking and computational complexity usually play a pivotal role, singularities in the solution or high regularity may dominate the choice for the method and the mesh-design. The first academic numerical example on the unit square is designed such that the linear P_1 finite element shows locking. The experiments with several Poisson ratios v close to 1/2 confirm the theoretical locking-free property of the symmetric MFEM. The theoretical findings of [9], that P_k, $k = 1, 2, 3$, show locking while P_4 is locking free, are empirically verified. For this smooth example the higher-order schemes show faster convergence rates and higher accuracy. However, this example is not representative from a practical point of view. Experiments for the Cook's membrane and the example with rigid circular inclusion show that singular solutions or curved boundaries can reduce the convergence rates of the methods. For the Cook's membrane problem even the low-order schemes lead to suboptimal convergence rates. This motivates the use of local mesh refinement which is investigated more closely for some L-shaped domain. The experiments show that graded meshes in contrast to uniform meshes lead to optimal

Table 2
Theoretical convergence rates of different mixed FEM, the non-conforming KS-FEM and the conforming P_k-FEM. The constant C is independent of material parameters (except for P_k, $k = 1, 2, 3$) and independent of the (sufficiently small) mesh size h.

Name	Convergence result
AW21	$\|\sigma - \sigma_h\|_{L^2(\Omega)} \leqslant Ch\|u\|_{H^2(\Omega)}$
AW15	$\|\sigma - \sigma_h\|_{L^2(\Omega)} \leqslant Ch\|u\|_{H^2(\Omega)}$
AW30	$\|\sigma - \sigma_h\|_{L^2(\Omega)} \leqslant Ch^m\|\sigma\|_{H^m(\Omega)}$ for $1 \leqslant m \leqslant 3$
AW24	$\|\sigma - \sigma_h\|_{L^2(\Omega)} \leqslant Ch^m\|\sigma\|_{H^m(\Omega)}$ for $1 \leqslant m \leqslant 2$
S15	$\|\sigma - \sigma_h\|_{L^2(\Omega)} \leqslant Ch^{m-1}\|u\|_{H^m(\Omega)}$ for $1 \leqslant m \leqslant 2$
S27	$\|\sigma - \sigma_h\|_{L^2(\Omega)} \leqslant Ch^{m-1}\|u\|_{H^m(\Omega)}$ for $1 \leqslant m \leqslant 3$
KS	$\|\sigma - \sigma_h\|_{L^2(\Omega)} \leqslant Ch\|\sigma\|_{H^1(\Omega)}$
PEERS	$\|\sigma - \sigma_h\|_{L^2(\Omega)} \leqslant Ch\|\sigma\|_{H^1(\Omega)}$
P_k	$\|\sigma - \sigma_h\|_{L^2(\Omega)} \leqslant C(\lambda)h^k\|u\|_{H^{k+1}(\Omega)}$ for $k = 1, 2, 3$
P_4	$\|\sigma - \sigma_h\|_{L^2(\Omega)} \leqslant Ch^4\|u\|_{H^5(\Omega)}$

convergence rates. However, the right choice of the grading parameter is not known in practise because it depends on the material parameters. The experiments show that a too small grading parameter results in suboptimal convergence rates while a too large value can lead to errors of different order of magnitude in accuracy. Therefore adaptive mesh refinement strategies for the symmetric MFEM have to be investigated which is postponed to forthcoming work.

The problem we are concerned with in this paper is assumed on some plane elastic body $\Omega \subset \mathbb{R}^2$ with boundary $\partial\Omega = \Gamma = \Gamma_D \cap \Gamma_N$ which consists of some closed part Γ_D of positive length for displacement boundary conditions u_D and its complement $\Gamma_N = \Gamma \setminus \Gamma_D$ subject to surface loads g with exterior unit normal ν. Given a volume force $f \in L^2(\Omega;\mathbb{R}^2)$ and a traction $g \in L^2(\Gamma_N;\mathbb{R}^2)$, we seek the displacement field $u \in \mathcal{V} := L^2(\Omega;\mathbb{R}^2)$ and the stress tensor $\sigma \in \Sigma := H(\mathrm{div},\Omega;\mathbb{S})$ which satisfy

$$\begin{aligned} &-\mathrm{div}\sigma = f \quad \text{and} \quad \sigma = \mathbb{C}\varepsilon(u) \quad \text{in} \quad \Omega,\\ &u = u_D \quad \text{on} \quad \Gamma_D \quad \text{and} \quad \sigma\nu = g \quad \text{on} \quad \Gamma_N. \end{aligned} \tag{1.1}$$

Here and throughout this paper, $\varepsilon(v) := \mathrm{sym}Dv$ is the linearised Green strain tensor and $\mathbb{C}$ is the symmetric fourth-order bounded and positive definite isotropic elasticity tensor. In computations, we seek an approximation $(\sigma_h, u_h) \in \Sigma_h \times \mathcal{V}_h$ in possible discrete spaces Σ_h and $\mathcal{V}_h$ discussed in detail in the next section. The standard notation for Lebesgue spaces $L^2(\Omega)$ and Sobolev spaces $H^1(\Omega)$ is used throughout the paper. Additionally, in the context of the examined Lamé problem described above, $\mathbb{S} := \mathbb{R}^{2\times 2}_{\mathrm{sym}}$ denotes the space of symmetric matrices.

The paper is organised as follows: Section 2 outlines the design and implementation of the two non-conforming Arnold–Winther MFEM [7] as a continuation of the examinations in [13] for the conforming MFEM of [5]. Since the formulation of the MFEM by Schöberl and Sinwel [18] is similar to the former MFEM, we suggest a new design of the base functions. The computational competition in Section 3 compares the four Arnold–Winther and two Schöberl–Sinwel symmetric MFEM to the weakly symmetric PEERS MFEM and the KS and P_k, $k = 1, 2, 3, 4$, displacement FEM. Section 4 outlines some conclusions.

2. Mixed non-conforming finite element formulation

This section summarises the design of the non-conforming mixed finite element AW21 and the simplified AW15 finite element of [7]. We detail the derivation of the coefficient matrices which determine the discrete basis functions and comment on the discretisation of the (local) operator matrices.

We assume some regular triangulation $\mathcal{T} \subset \Omega \subset \mathbb{R}^2$ with the set of edges $\mathcal{E}$ and the set of nodes $\mathcal{N}$, i.e., it holds for any triangles $T_1, T_2 \in \mathcal{T}$

$$T_1 \cap T_2 \in \mathcal{T} \cup \mathcal{E} \cup \mathcal{N} \cup \{\emptyset\}.$$

Unit outer normal and tangent vectors with respect to an edge $E \in \mathcal{E}$ are then defined to be ν_E and τ_E, respectively.

In addition to the spaces defined above, the spaces

$$\Sigma_0 := \left\{\sigma \in H(\mathrm{div},\Omega;\mathbb{S}) \middle| \int_{\Gamma_N} \psi\cdot(\sigma\nu)\,ds = 0 \text{ for all } \psi \in \mathcal{D}(\Gamma_N;\mathbb{R}^2)\right\},$$

$$\begin{aligned}\Sigma_g := \{&\sigma \in H(\mathrm{div},\Omega;\mathbb{S}) \middle| \int_{\Gamma_N} \psi\cdot(\sigma\nu)\,ds\\ &= \int_{\Gamma_N} \psi\cdot g\,ds \text{ for all } \psi \in \mathcal{D}(\Gamma_N;\mathbb{R}^2)\}\end{aligned}$$

involve the traction boundary conditions where $\mathcal{D}$ is the space of test functions.

The weak formulation of (1.1) reads: given data $u_D \in H^1(\Omega;\mathbb{R}^2)$, $f \in L^2(\Omega;\mathbb{R}^2)$, $g \in L^2(\Gamma_N;\mathbb{R}^2)$, seek the solution $(\sigma,u) \in \Sigma_g \times \mathcal{V}$ with

$$\begin{aligned} &\int_\Omega \sigma : \mathbb{C}^{-1}\tau\,dx + \int_\Omega u\cdot\mathrm{div}\tau\,dx = \int_{\Gamma_D} u_D\cdot(\tau\nu_\Omega)\,ds \quad \text{for all } \tau \in \Sigma_0,\\ &\int_\Omega v\cdot\mathrm{div}\sigma\,dx = -\int_\Omega f\cdot v\,dx \quad \text{for all } v \in \mathcal{V}. \end{aligned} \tag{2.1}$$

2.1. MFEM design (AW21)

According to [7], the discrete spaces for stress and displacement for the non-conforming mixed finite element denoted AW21 in Table 1 are defined on a triangle $T \in \mathcal{T} \subset \Omega$ by

$$\begin{aligned} &\Sigma_T := \{\sigma \in P_2(T,\mathbb{S}) \mid \nu_E\cdot(\sigma\nu_E) \in P_1(E) \text{ for each edge } E \in T\},\\ &\mathcal{V}_T := P_1(T,\mathbb{R}^2). \end{aligned} \tag{2.2}$$

For each triangle $T \in \mathcal{T}$ and the barycentric coordinates $\lambda_1, \lambda_2, \lambda_3$ on T a basis $(\varphi_1,\dots,\varphi_6)$ of $P_2(T;\mathbb{R})$ reads

$$\begin{aligned} &\varphi_1 = \lambda_1, \quad \varphi_2 = \lambda_2, \quad \varphi_3 = \lambda_3,\\ &\varphi_4 = \lambda_1\lambda_2, \quad \varphi_5 = \lambda_2\lambda_3, \quad \varphi_6 = \lambda_1\lambda_3. \end{aligned}$$

The 18 coefficients $a_1,\dots,a_6,b_1,\dots,b_6,c_1,\dots,c_6 \in \mathbb{R}$ of an arbitrary stress field $\sigma_T \in P_2(T;\mathbb{S})$ read

$$\sigma_T := \sum_{k=1}^{6} \varphi_k \begin{pmatrix} a_k & c_k\\ c_k & b_k\end{pmatrix}. \tag{2.3}$$

The 15 degrees of freedom $\xi_1,\dots,\xi_{15}$ of $\sigma_T \in \Sigma_T$ are specified according to (2.2) by the following.

(a) The values of the moments of degree 0 and 1 of the two normal components of σ on each edge E_1, E_2, E_3 of T (12 degrees of freedom), namely, for $j = 1, 2, 3$,

$$|E_j|^{-1}\int_{E_j} \sigma\nu_{E_j}\,ds = \begin{pmatrix}\xi_{4(j-1)+1}\\ \xi_{4(j-1)+2}\end{pmatrix},$$

$$|E_j|^{-2}\int_{E_j} ((x-\mathrm{mid}(E_j))\tau_{E_j})\sigma\nu_{E_j}\,ds = \begin{pmatrix}\xi_{4(j-1)+3}\\ \xi_{4(j-1)+4}\end{pmatrix}.$$

(b) The values of the three components of the integral mean of σ on T (3 degrees of freedom), i.e.,

$$|T|^{-1}\int_T \sigma\,dx = \begin{pmatrix}\xi_{13} & \xi_{15}\\ \xi_{15} & \xi_{14}\end{pmatrix}.$$

The coefficients of the basis functions in (2.3) for some triangle $T \in \mathcal{T}$ and $\sigma_T \in \Sigma_T$ are specified by the linear relation

$$C(a_1,b_1,c_1,\dots,a_6,b_6,c_6)^T = (\xi_1,\dots,\xi_{18})^T \tag{2.4}$$

with the 18×18 matrix C. By the definition (a)–(b) of the degrees of freedom and the constraints with regard to the considered stress space (2.2)

$$C := \frac{1}{60}\begin{pmatrix} R & S\\ 20\widetilde{I} & 5\widetilde{I}\\ 0 & 60K\end{pmatrix}.$$

The evaluation of the integrals in (a) for the P_2 basis yields the entries in the first row and involves the degrees of freedom $\xi_1,\dots,\xi_{12}$ given by

$$R := \begin{pmatrix} 30N^{(1)} & 30N^{(1)} & 0 \\ -5M^{(1)} & 5M^{(1)} & 0 \\ 0 & 30N^{(2)} & 30N^{(2)} \\ 0 & -5M^{(2)} & 5M^{(2)} \\ 30N^{(3)} & 0 & 30N^{(3)} \\ 5M^{(3)} & 0 & -5M^{(3)} \end{pmatrix},$$

$$S := \begin{pmatrix} 10N^{(1)} & 0 & 0 \\ 0 & 0 & 0 \\ 0 & 10N^{(2)} & 0 \\ 0 & 0 & 0 \\ 0 & 0 & 10N^{(3)} \\ 0 & 0 & 0 \end{pmatrix}$$

with the normals matrix

$$N^{(j)} := \begin{pmatrix} v_{E_j}(1) & 0 & v_{E_j}(2) \\ 0 & v_{E_j}(2) & v_{E_j}(1) \end{pmatrix} \in \mathbb{R}^{2\times 3}$$

for the kth component $v_{E_j}(k)$ of the global unit normal v_{E_j} along the jth edge E_j of a triangle T. We define the element-dependent normals matrix M which is identical to N with the difference that, instead of unique global normal vectors, it contains the outer unit normals along the edges of the elements. The conditions (b) for degrees of freedom $\xi_{13},\dots,\xi_{15}$ are encoded in the second row of C with 3×3 identity matrices $I_{3\times 3}$ and

$$\widetilde{I} := (I_{3\times 3}\ I_{3\times 3}\ I_{3\times 3}) \in \mathbb{R}^{3\times 9}.$$

Since any stress field $\sigma_T \in \Sigma_T$ has to satisfy $v_{E_j}\cdot(\sigma v_{E_j}) \in P_1(E_j)$ on the edges E_1,E_2,E_3 of T, the remaining degrees of freedom $\xi_{16},\dots,\xi_{18}$ vanish and the respective conditions are included in C by

$$K^{(j)} := ((v_{E_j}(1))^2,\ (v_{E_j}(2))^2,\ 2v_{E_j}(1)v_{E_j}(2)) \in \mathbb{R}^3$$

with

$$K := \begin{pmatrix} K^{(1)} & 0 & 0 \\ 0 & K^{(2)} & 0 \\ 0 & 0 & K^{(3)} \end{pmatrix} \in \mathbb{R}^{3\times 9}.$$

2.2. Local stiffness matrix (AW21)

The fourth-order material tensor $\mathbb{C}$ and its inverse $\mathbb{C}^{-1}$ read

$$\mathbb{C} := \begin{pmatrix} 2\mu+\lambda & \lambda & 0 \\ \lambda & 2\mu+\lambda & 0 \\ 0 & 0 & \mu \end{pmatrix}, \quad \mathbb{C}^{-1} := \begin{pmatrix} \frac{\lambda+2\mu}{4\mu(\lambda+\mu)} & \frac{-\lambda}{4\mu(\lambda+\mu)} & 0 \\ \frac{-\lambda}{4\mu(\lambda+\mu)} & \frac{\lambda+2\mu}{4\mu(\lambda+\mu)} & 0 \\ 0 & 0 & \frac{1}{\mu} \end{pmatrix}.$$

On each triangle $T\in\mathcal{T}$ the local stiffness matrix, resulting from (2.1),

$$\mathrm{STIMA}(T) := \begin{pmatrix} A & B \\ B^T & 0 \end{pmatrix} \in \mathbb{R}^{21\times 21}_{\mathrm{sym}}$$

requires the computation of

$$A_{jk} := \int_T \sigma_j : \mathbb{C}^{-1}\sigma_k \, dx \quad \text{for } j,k = 1,\dots,15; \tag{2.5a}$$

$$B_{jk} := \int_T \mathrm{div}\sigma_j \cdot v_k \, dx \quad \text{for } j = 1,\dots,15;\ k = 1,\dots,6. \tag{2.5b}$$

Any basis function $\sigma_1,\dots,\sigma_{15}$ of Σ_T resulting from the coefficient evaluation in (2.4) can be represented as

$$\sigma_j = \begin{pmatrix} \alpha_j & \gamma_j \\ \gamma_j & \beta_j \end{pmatrix} \quad \text{and} \quad \begin{pmatrix} \alpha_j \\ \beta_j \\ \gamma_j \end{pmatrix} := \begin{pmatrix} \sum_{k=1}^6 a_j^{(k)}\varphi_k \\ \sum_{k=1}^6 b_j^{(k)}\varphi_k \\ \sum_{k=1}^6 c_j^{(k)}\varphi_k \end{pmatrix}.$$

The entry A_{jk} of the local stiffness matrix is given for the base functions σ_j and σ_k by

$$\begin{aligned} A_{jk} &= \int_T \sigma_j : \mathbb{C}^{-1}\sigma_k \, dx = \int_T (\alpha_j,\beta_j,\gamma_j)\mathbb{C}^{-1}(\alpha_k,\beta_k,\gamma_k)^T \, dx \\ &= \mathbb{C}^{-1}_{1,1}\int_T (\alpha_j\alpha_k+\beta_j\beta_k)\, dx + \mathbb{C}^{-1}_{1,2}\int_T (\alpha_j\beta_k+\beta_j\alpha_k)\, dx \\ &\quad + \mathbb{C}^{-1}_{3,3}\int_T \gamma_j\gamma_k \, dx. \end{aligned}$$

The integrals occurring in the A_{jk} can be integrated exactly on any $T\in\mathcal{T}$

$$\int_T \alpha_j\beta_k \, dx = \sum_{m=1}^6\sum_{n=1}^6 a_m^{(j)}b_n^{(k)}\int_T \varphi_m\varphi_n \, dx = |T| a^{(j)^T} M b^{(k)}$$

with the mass matrix

$$M := \frac{1}{180}\begin{pmatrix} 30 & 15 & 15 & 6 & 3 & 6 \\ 15 & 30 & 15 & 6 & 6 & 3 \\ 15 & 15 & 30 & 3 & 6 & 6 \\ 6 & 6 & 3 & 2 & 1 & 1 \\ 3 & 6 & 6 & 1 & 2 & 1 \\ 6 & 3 & 6 & 1 & 1 & 2 \end{pmatrix}.$$

For the evaluation of the second part of the stiffness matrix (2.5b) we recall the conditions imposed on elements of Σ_T and note that the divergence of any base function σ_j yields the form

$$\mathrm{div}\sigma_j = \begin{pmatrix} d_1^{(j)}\varphi_1 + d_3^{(j)}\varphi_2 + d_5^{(j)}\varphi_3 \\ d_2^{(j)}\varphi_1 + d_4^{(j)}\varphi_2 + d_6^{(j)}\varphi_3 \end{pmatrix}$$

for some coefficients $d_k^{(j)}$. From this we derive the coefficient matrix $D := (d^{(1)},\dots,d^{(18)})$ given by

$$D := \begin{pmatrix} L_1 & L_2 & L_3 & L_2 & 0 & L_3 \\ L_1 & L_2 & L_3 & L_1 & L_3 & 0 \\ L_1 & L_2 & L_3 & 0 & L_2 & L_1 \end{pmatrix} X$$

with the derivative matrices L_1, L_2, L_3,

$$L_k := \begin{pmatrix} D_x\lambda_k & 0 & D_y\lambda_k \\ 0 & D_y\lambda_k & D_x\lambda_k \end{pmatrix}$$

and

$$X = (x^{(1)},\dots,x^{(15)}) \in \mathbb{R}^{18\times 15},$$
$$x^{(j)} = \left(a_1^{(j)}, b_1^{(j)}, c_1^{(j)}, \dots, a_6^{(j)}, b_6^{(j)}, c_6^{(j)}\right)^T \in \mathbb{R}^{18}.$$

The second part of the stiffness matrix (2.5b) reads

$$B := \frac{|T|}{12}\begin{pmatrix} 2 & 1 & 1 & 0 & 0 & 0 \\ 1 & 2 & 1 & 0 & 0 & 0 \\ 1 & 1 & 2 & 0 & 0 & 0 \\ 0 & 0 & 0 & 2 & 1 & 1 \\ 0 & 0 & 0 & 1 & 2 & 1 \\ 0 & 0 & 0 & 1 & 1 & 2 \end{pmatrix}\begin{pmatrix} 1 & 0 & 0 & 0 & 0 & 0 \\ 0 & 0 & 1 & 0 & 0 & 0 \\ 0 & 0 & 0 & 0 & 1 & 0 \\ 0 & 1 & 0 & 0 & 0 & 0 \\ 0 & 0 & 0 & 1 & 0 & 0 \\ 0 & 0 & 0 & 0 & 0 & 1 \end{pmatrix} D.$$

Remark 2.1. Neumann boundary condition are essential conditions in the mixed formulation (2.1) and have to be imposed on the discrete stresses. Opposite to the treatment with Lagrange multipliers in [13], the current implementation eliminates respective boundary degrees of freedom by condensation.

2.3. MFEM design (AW15)

In addition to the element described above, a simplified non-conforming element was derived in [7] which only includes the reduced velocity space $\mathcal{V}_T := \mathrm{RM}(T)$ of discontinuous piecewise rigid body motions, see AW15 in Table 1. More specifically, a function in $\mathrm{RM}(T)$ has a representation $(a, b)^T + c(-y, x)^T$ for some coefficients $a, b, c \in \mathbb{R}$. The reduced local stress space $\widehat{\Sigma}_T$ is given by

$$\widehat{\Sigma}_T := \{\tau \in \Sigma_T | \mathrm{div}\tau \in \mathrm{RM}(T)\}.$$

When compared to the non-conforming element of Section 2.1, the degrees of freedom corresponding to the first two moments of the normal derivatives on the edges are still used while the integral mean values on the element were dropped. Moreover, the constraint on the divergence of the stress fields now is more restricted by means of the space $\mathrm{RM}(T)$.

In order to obtain the unknown coefficients $a_1, b_1, c_1, \ldots, a_6, b_6, c_6$ of the basis functions for a discrete $\sigma_T \in \widehat{\Sigma}_T$ on a triangle T, we solve a linear system

$$C(a_1, b_1, c_1, \ldots, a_6, b_6, c_6)^T = (\xi_1, \ldots, \xi_{18})^T. \tag{2.6}$$

The constraints of $\widehat{\Sigma}_T$ lead to the coefficient matrix

$$C := \frac{1}{60}\begin{pmatrix} R & S \\ 0 & 60\widetilde{Q} \\ 0 & 60K \end{pmatrix} \in \mathbb{R}^{18\times 18}$$

which encodes 12 base functions in terms of the aforementioned P_2 basis. The first row represents the degrees of freedom resulting from the first two moments of the normal derivatives on the edges of a triangle with matrices $R, S \in \mathbb{R}^{12\times 9}$ from Section 2.1. The constraints of the space RM are encoded in the second row of C by means of the matrix

$$Q^{(j)} := \mathrm{diam}(T)\begin{pmatrix} D_x v^{(j)} & 0 & D_y v^{(j)} \\ 0 & D_y w^{(j)} & D_x w^{(j)} \\ D_x w^{(j)} & D_y v^{(j)} & D_y w^{(j)} + D_x v^{(j)} \end{pmatrix}$$

with

$$v^{(1)\cdots(3)} := ((\lambda_1 - \lambda_2), \lambda_3, -\lambda_3),$$
$$w^{(1)\cdots(3)} := (-\lambda_2, \lambda_2, (\lambda_1 - \lambda_3)),$$
$$\widetilde{Q} := (Q^{(1)}, Q^{(2)}, Q^{(3)}) \in \mathbb{R}^{3\times 9}.$$

Note that the matrix $\widetilde{Q}$ is scaled in relation to the size of the triangle in order to avoid ill-conditioning of the coefficient matrix. The remaining vanishing quadratic degrees of freedom are encoded in the matrix $K \in \mathbb{R}^{3\times 9}$ from Section 2.1.

2.4. Local stiffness matrix (AW15)

The evaluation of the local stiffness matrix follows the derivation in Section 2.2. While A is evaluated as before, by definition of the base functions and the constraints on the stress space, the divergence of some σ_j has the form

$$\mathrm{div}\sigma_j = \begin{pmatrix} d_1^j - d_3^j\varphi_3 \\ d_2^j + d_3^j\varphi_2 \end{pmatrix}$$

for some coefficients $d_k^{(j)} \in \mathbb{R}$. The coefficient matrix $D := (d^{(1)}, \ldots, d^{(15)})$ reads

$$D := \begin{pmatrix} F_1 & F_2 & F_3 & F_2 & 0 & F_3 \\ G_1 & G_2 & G_3 & G_2 & 0 & G_3 \\ 0 & 0 & 0 & G_1 - G_2 & G_3 & -G_3 \end{pmatrix} X$$

with

$$F_k := (D_x\lambda_k \; 0 \; D_y\lambda_k),$$
$$G_k := (0 \; D_y\lambda_k \; D_x\lambda_k)$$

and

$$X = (x^{(1)}, \ldots, x^{(12)}) \in \mathbb{R}^{18\times 12},$$
$$x^{(j)} = \left(a_1^{(j)}, b_1^{(j)}, c_1^{(j)}, \ldots, a_6^{(j)}, b_6^{(j)}, c_6^{(j)}\right)^T \in \mathbb{R}^{18}.$$

The second part of the stiffness matrix simplifies to

$$B := \frac{|T|}{3}\begin{pmatrix} 3 & 0 & -1 \\ 0 & 3 & 1 \\ -1 & 1 & 1 \end{pmatrix} D.$$

2.5. Other symmetric MFEM

In addition to providing details about the implementation of the non-conforming Arnold–Winther elements in the previous section, we also aim to compare it to other symmetric MFEM developed recently. A detailed account on the conforming Arnold–Winther element [5] was given in [13] and we only summarise the main properties for the sake of completeness. Another set of symmetric element is due to [18]. Instead of using the explicit base functions listed in the reference, our implementation follows the lines of the Arnold–Winther element implementation. It thus is instructive to provide some details about the required modifications for the design of the shape functions.

2.5.1. Conforming Arnold–Winther elements

The conforming elements of Arnold and Winther for the mixed formulation are based on polynomials of degree 3 for the symmetric stresses and of degree 1 for the displacement, see AW30 and AW24 in Table 1. In order to obtain continuity of the stress field in normal direction along the boundary of elements, it was shown in [5] that vertex degrees of freedom cannot be circumvented. The non-conforming elements AW21 and AW15 described above on the one hand lack normal-stress continuity due to missing vertex degrees of freedom which, on the other hand, enables to employ a lower polynomial degree for the stress space. For the conforming AW30 element, a reduced AW24 element was described as well. Since the design of the AW24 element is similar to the one of the AW30 element [13] and to the ones presented above, we omit the details. Experimental results for the two lowest order conforming Arnold–Winther elements as depicted in Table 1 are presented in Section 3.

2.5.2. Schöberl–Sinwel TD-NNS Elements

In [18], a class of mixed finite elements were presented which employ subspaces of $H(\mathrm{curl}, \Omega; \mathbb{R}^2)$ for the displacement and of $H(\mathrm{divdiv}, \Omega; \mathbb{S})$ for the stress. According to the continuity requirements, the method is coined Tangential-Displacement-Normal-Normal-Stress (TD-NNS) formulation of elasticity. In this paper, for the sake of simpler notation, we call these elements S15 and S27 of polynomial degree 1 and 2 and overall number of degrees of freedom 15 and 27 as depicted in Table 1 for comparison with Arnold–Winther elements. The homogeneous spaces of order k are defined by

$$\Sigma_{h,k} := \{\sigma \in L^2_{\mathrm{sym}}(\Omega) \mid \sigma|_T \in P_k(T; \mathbb{S}), \quad v_E \cdot (\sigma v_E) = 0 \text{ on } \Gamma_N$$
$$\forall E \in \partial T : v_E \cdot (\sigma v_E) \in P_{\max(1,k-1)}(E) \cap C^0(\Omega)\},$$
$$\mathcal{V}_{h,k} := \{v \in L^2(\Omega)^2 \mid v|_T \in P_k(T; \mathbb{R}^2), \; v \cdot \tau_E \in C^0(\Omega), \; v \cdot \tau_E = 0 \text{ on } \Gamma_D\}.$$

Note that $\mathcal{V}_{h,k}$ is the second family of Nédélec edge elements. The homogeneous problem is given by: find $(\sigma,u)\in\Sigma_{h,k}\times\mathcal{V}_{h,k}$ such that

$$\begin{aligned} a(\sigma,\rho)+b(\rho,u)&=0 \qquad \forall\rho\in\Sigma_{h,k},\\ b(\sigma,v)&=-(f,v) \quad \forall v\in\mathcal{V}_{h,k}\end{aligned}$$

with the bilinear forms

$$a(\sigma,\rho):=\int_\Omega \sigma:\mathbb{C}^{-1}\rho\ dx,$$

$$b(\rho,v):=\langle \mathrm{div}\rho,v\rangle=\sum_{T\in\mathcal{T}}\int_T \mathrm{div}\rho\cdot v\ dx-\int_{\partial T}(\tau\cdot(\rho\nu))(v\cdot\tau)\ ds.$$

Opposite to the basis functions derived in [18], we prefer an approach similar to the design of the Arnold–Winther mixed FEM presented above and in [13]. In what follows, we discuss the design of the S27 element of order 2. The design of the order 1 element S15 is a mere reduction of the shown approach.

As in Section 2.3, some stress field $\sigma_T\in P_k(T;\mathbb{S})$ and some displacement field $u_T\in P_k(T;\mathbb{R}^2)$ on some triangle T have the form

$$\sigma_T:=\sum_{j=1}^{N_k}\varphi_j\begin{pmatrix}a_k & c_k\\ c_k & b_k\end{pmatrix}\quad\text{and}\quad u_T:=\sum_{j=1}^{N_k}\varphi_j\begin{pmatrix}d_k\\ e_k\end{pmatrix}$$

with $(3+2)N_k$ coefficients overall, according to degree k of the polynomial space. The 15 + 12 degrees of freedom for the S27 element are defined by (a)–(d).

(a) The values of the moments of degree 0 and 1 of the two normal–normal components of σ on each edge E_1,E_2,E_3 of T (6 degrees of freedom), namely, for $j=1,2,3$,

$$|E_j|^{-1}\int_{E_j}(\sigma\nu_{E_j})\cdot\nu_{E_j}\ ds=\xi_{2(j-1)+1},$$

$$|E_j|^{-2}\int_{E_j}((x-\mathrm{mid}(E_j))\tau_{E_j})(\sigma\nu_{E_j})\cdot\nu_{E_j}\ ds=\xi_{2(j-1)+2}.$$

(b) The values of the three components of the integral mean of σ on T tested with a basis $\{\varphi_j\}$ of $P_1(T;\mathbb{S})$ (9 degrees of freedom)

$$|T|^{-1}\int_T \sigma\ :\ \varphi_j\ dx=\xi_{j+6}\quad\text{for}\quad j=1,\dots,9.$$

For instance a basis of $P_1(T;\mathbb{S})$ is given by $\left\{\begin{pmatrix}\lambda_k & 0\\ 0 & 0\end{pmatrix},\begin{pmatrix}0 & 0\\ 0 & \lambda_k\end{pmatrix},\frac{1}{2}\begin{pmatrix}0 & \lambda_k\\ \lambda_k & 0\end{pmatrix}\right\},\quad k=1,2,3.$

(c) The values of the moments of degrees 0, 1 and 2 of the tangential components of u on each edge E_1,E_2,E_3 of T (9 degrees of freedom), namely, for $j=1,2,3$,

$$|E_j|^{-1}\int_{E_j}u\cdot\tau_{E_j}\ ds=\xi_{3(j-1)+16},$$

$$|E_j|^{-2}\int_{E_j}((x-\mathrm{mid}(E_j))\tau_{E_j})u\cdot\tau_{E_j}\ ds=\xi_{3(j-1)+17},$$

$$|E_j|^{-3}\int_{E_j}((x-\mathrm{mid}(E_j))\tau_{E_j})^2u\cdot\tau_{E_j}\ ds=\xi_{3(j-1)+18}.$$

(d) The values of the integral mean on the element tested with a basis $\{q_j\}$ of the space $P_0(T;\mathbb{R}^2)\oplus xP_0(T)$ such as $\left\{\begin{pmatrix}1\\0\end{pmatrix},\begin{pmatrix}0\\1\end{pmatrix},\begin{pmatrix}\lambda_2\\ \lambda_3\end{pmatrix}\right\}$ (3 degrees of freedom)

$$|T|^{-1}\int_T u\cdot q_j\ dx=\xi_{j+24}\quad\text{for j = 1, 2, 3.}$$

With the notation from Section 2.1 the coefficient matrix for the stress space $\Sigma_T:=\Sigma_{h,2}|_T$ reads

$$C_{\Sigma_T}:=\frac{1}{60}\begin{pmatrix}R & S\\ I_R & I_S\\ 0 & 60K\end{pmatrix}\in\mathbb{R}^{18\times18}.$$

It is formed according to the moments and constraints described in (a) and (b). The evaluation of the integrals in (a) for the P_2 basis yields the entries in the first row and involves the degrees of freedom $\xi_1,\dots,\xi_6$ given by

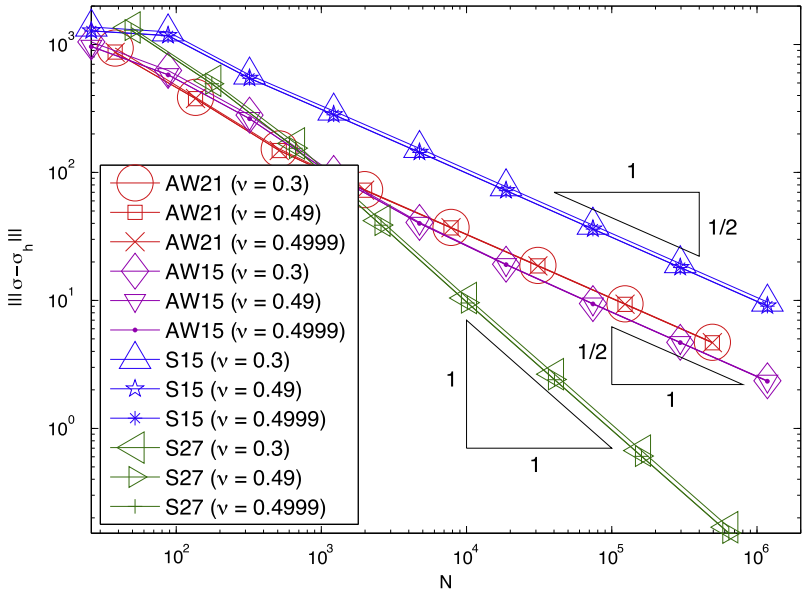

Fig. 3.1. Energy error $|||\sigma-\sigma_h|||$ for the academic example with Poisson ratio $\nu=0.3, 0.49, 0.4999$.

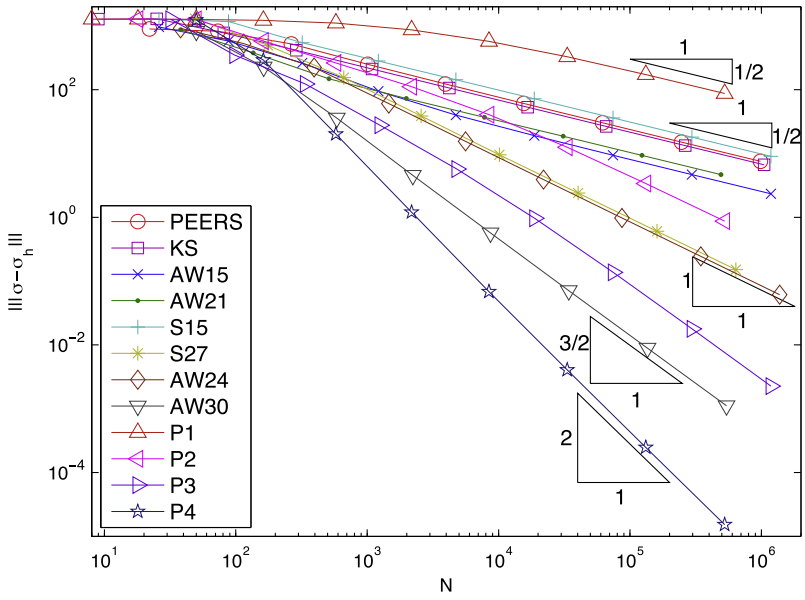

Fig. 3.2. Survey of the energy error $|||\sigma - \sigma_h|||$ for the academic example with Poisson ratio $\nu = 0.499$.

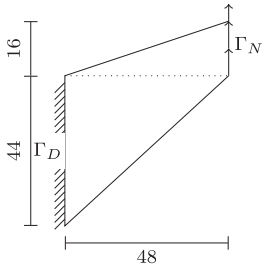

Fig. 3.3. The Cook's membrane.

$$R := \begin{pmatrix} 30N^{(1)} & 30N^{(1)} & 0 \\ -5M^{(1)} & 5M^{(1)} & 0 \\ 0 & 30N^{(2)} & 30N^{(2)} \\ 0 & -5M^{(2)} & 5M^{(2)} \\ 30N^{(3)} & 0 & 30N^{(3)} \\ 5M^{(3)} & 0 & -5M^{(3)} \end{pmatrix},$$

$$S := \begin{pmatrix} 10N^{(1)} & 0 & 0 \\ 0 & 0 & 0 \\ 0 & 10N^{(2)} & 0 \\ 0 & 0 & 0 \\ 0 & 0 & 10N^{(3)} \\ 0 & 0 & 0 \end{pmatrix}$$

with the normal–normal vectors

$$N^{(j)} := ((v_{E_j}(1))^2,\ (v_{E_j}(2))^2,\ 2v_{E_j}(1)v_{E_j}(2)) \in \mathbb{R}^3$$

for the kth component $v_{E_j}(k)$ of the globally unique normal v_{E_j} along the jth edge E_j of a triangle T. As mentioned before in Section 2.1, the matrix M contains the normal-normal entries with element-dependent outer unit normals. The conditions (b) for degrees of freedom $\xi_7, \ldots, \xi_{15}$ are encoded in the second row of C_{Σ_T} with 3×3 identity matrices I and

$$I_R := \begin{pmatrix} 10I & 5I & 5I \\ 5I & 10I & 5I \\ 5I & 5I & 10I \end{pmatrix} \quad \text{and} \quad I_S := \begin{pmatrix} 2I & 1I & 2I \\ 2I & 2I & 1I \\ 1I & 2I & 2I \end{pmatrix} \in \mathbb{R}^{9\times 9}.$$

The constraints $v_{E_j} \cdot (\sigma v_{E_j}) \in P_1(E_j)$ are encoded in the matrix $K \in \mathbb{R}^{3\times 9}$ from Section 2.1. Note that the coefficient matrix C_{Σ_T} is somehow similar to the one for the non-conforming Arnold–Winther elements.

The coefficient matrix

$$C_{\mathcal{V}_T} := \frac{1}{120}\begin{pmatrix} \widetilde{R} & \widetilde{S} \\ \widetilde{I}_R & \widetilde{I}_S \end{pmatrix} \in \mathbb{R}^{12\times 12}$$

corresponds to the displacement degrees of freedom described in (c) and (d). The evaluation of the integrals in (c) for the P_2 basis yields the entries in the first row and involves the degrees of freedom $\xi_{16}, \ldots, \xi_{24}$ given by

$$\widetilde{R} := \begin{pmatrix} 60N^{(1)} & 60N^{(1)} & 0 \\ -10M^{(1)} & 10M^{(1)} & 0 \\ 5N^{(1)} & 5N^{(1)} & 0 \\ 0 & 60N^{(2)} & 60N^{(2)} \\ 0 & -10M^{(2)} & 10M^{(2)} \\ 0 & 5N^{(2)} & 5N^{(2)} \\ 60N^{(3)} & 0 & 60N^{(3)} \\ 10M^{(3)} & 0 & -10M^{(3)} \\ 5N^{(3)} & 0 & 5N^{(3)} \end{pmatrix},$$

$$\widetilde{S} := \begin{pmatrix} 20N^{(1)} & 0 & 0 \\ 0 & 0 & 0 \\ N^{(1)} & 0 & 0 \\ 0 & 20N^{(2)} & 0 \\ 0 & 0 & 0 \\ 0 & N^{(2)} & 0 \\ 0 & 0 & 20N^{(3)} \\ 0 & 0 & 0 \\ 0 & 0 & N^{(3)} \end{pmatrix}$$

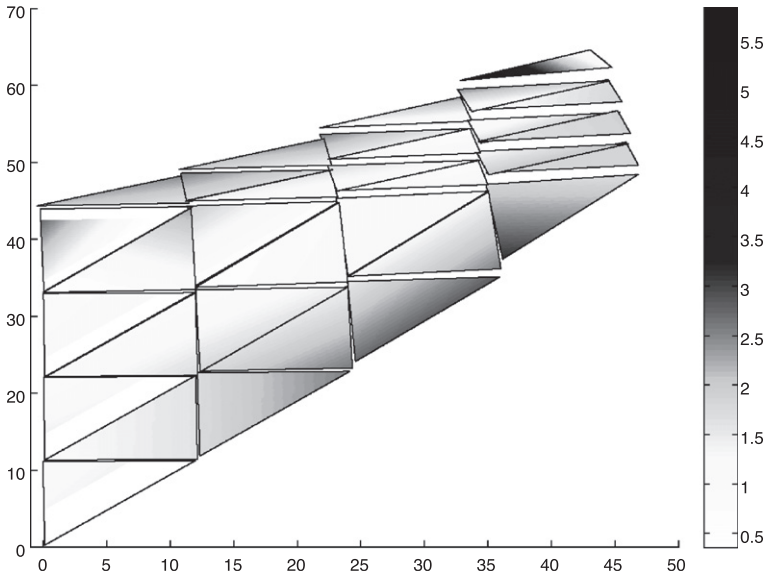

Fig. 3.4. Solution of the Cook's membrane benchmark.

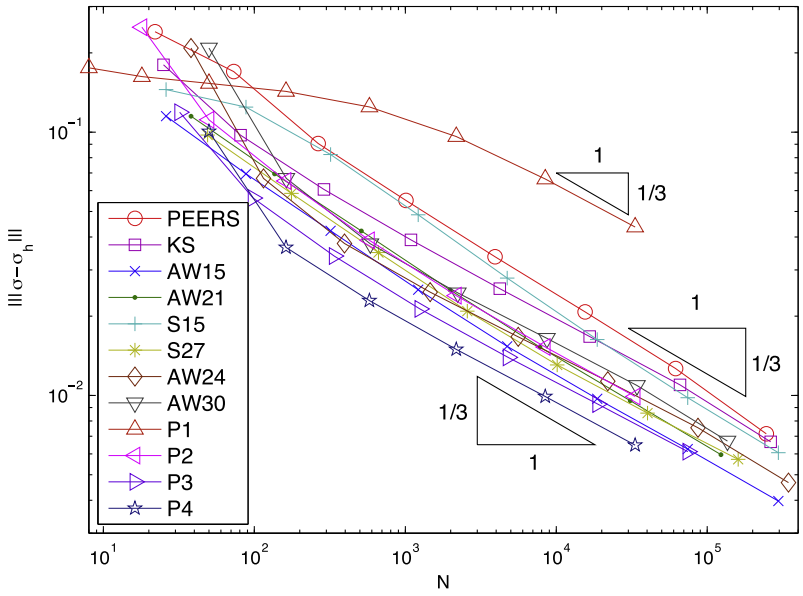

Fig. 3.5. Energy errors $|||\sigma - \sigma_h|||$ for the Cook's membrane problem with Poisson ratio $\nu = 0.499$.

with the global transpose tangents

$$N^{(j)} := (-v_{E_j}(2),\ v_{E_j}(1)) \in \mathbb{R}^2$$

and the element-dependent equivalent M. The conditions (d) for degrees of freedom $\xi_{25}, \ldots, \xi_{27}$ are encoded in the second row of $C_{\mathcal{V}_T}$ and

$$\widetilde{I}_R := \begin{pmatrix} 40 & 0 & 40 & 0 & 40 & 0 \\ 0 & 40 & 0 & 40 & 0 & 40 \\ 10 & 10 & 20 & 10 & 10 & 20 \end{pmatrix},$$

$$\widetilde{I}_S := \begin{pmatrix} 10 & 0 & 10 & 0 & 10 & 0 \\ 0 & 10 & 0 & 10 & 0 & 10 \\ 4 & 2 & 4 & 4 & 2 & 4 \end{pmatrix} \in \mathbb{R}^{3\times 6}.$$

3. Numerical experiments

This section presents the computational competition of the standard continuous P_k, $k = 1, \ldots, 4$, displacement finite elements, the weakly symmetric mixed finite element PEERS [2], the nonconforming displacement finite element KS [17] and the symmetric mixed methods AW30, AW24, AW21, AW15, S15 and S27 described above. We begin with an academic example which represents an ideal benchmark for the locking phenomenon. Next more realistic benchmark problems such as the Cook's membrane problem and the example of a rigid circular inclusion in an infinite plate are considered. Finally, the rotated L-shaped domain with singular solution motivates the need of local mesh refinement.

All methods will be compared with respect to the stress tensor error in the energy norm $|||\sigma||| := \|\mathbb{C}^{-1/2}(\sigma)\|_{L^2(\Omega)}$. The implementation of the AW30 MFEM is presented in [13] and due to the close relationship, a few modifications lead to an implementation of the AW24 MFEM. The implementation of PEERS is described in [11], where the continuity constraints are enforced using Lagrange multipliers. In order to compare the results of PEERS to all other methods, the error is plotted with respect to the theoretically necessary degrees of freedom and not to the size of the discrete system involving a high number of degrees of

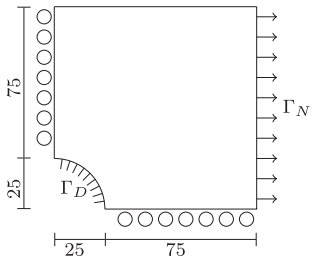

Fig. 3.6. Domain circular inclusion.

freedom for the Lagrange multipliers. For the KS non-conforming finite element, the first component is chosen to be non-conforming and the second component is chosen to be continuous. Note that in [9] it is proven that P_k shows locking for $k = 1, 2, 3$ and is locking free for $k = 4$, which is also confirmed by the following numerical examples.

Throughout this section, let N denote the number of degrees of freedom, i.e., the number of unknowns of the algebraic systems to be solved.

3.1. Academic example

As a first academic example consider the model problem (1.1) on the unit square $\Omega = (0,1) \times (0,1)$ with homogeneous Dirichlet boundary conditions. The elasticity modulus is set to $E = 10^5$ and the Poisson ratio is chosen out of $\nu \in \{0.3, 0.49, 0.4999\}$. The right hand side is defined as

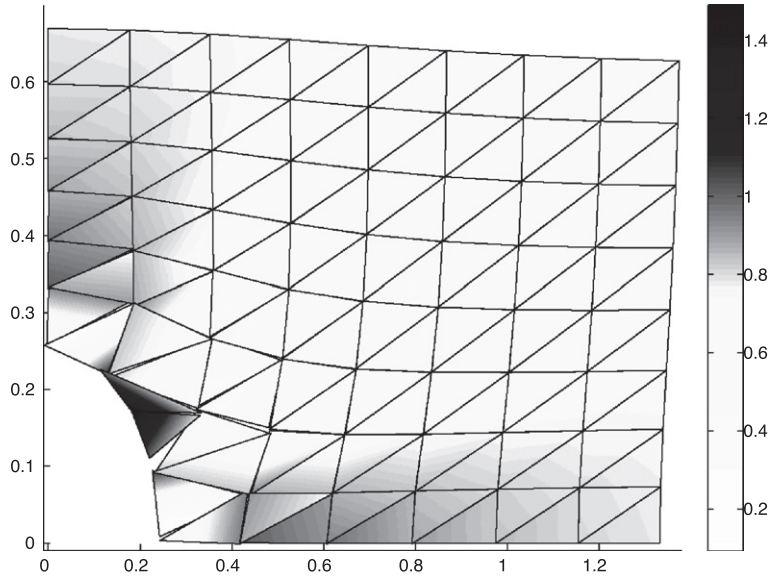

Fig. 3.7. Solution of the circular inclusion benchmark.

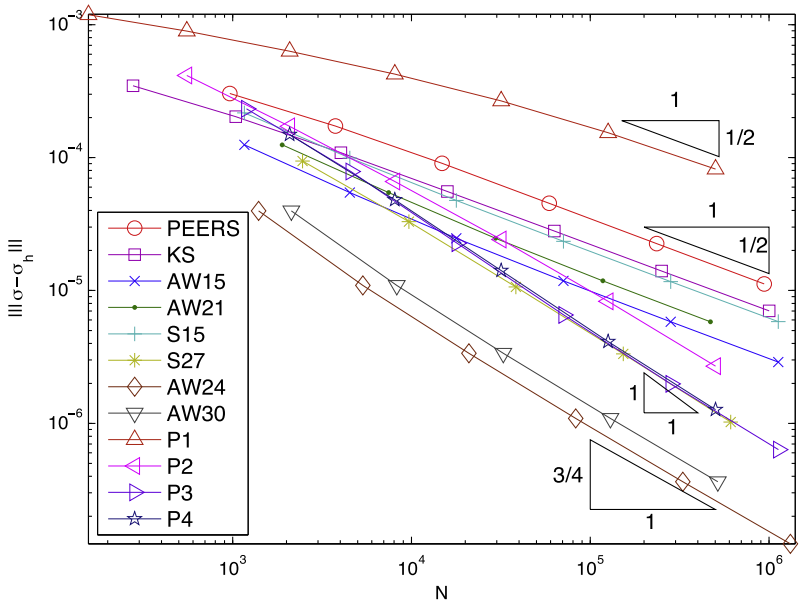

Fig. 3.8. Energy errors $|||\sigma - \sigma_h|||$ for the circular inclusion example with Poisson ratio $\nu = 0.499$.

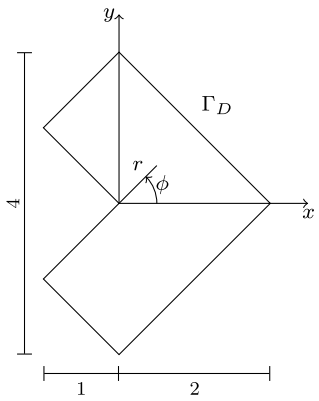

Fig. 3.9. The L-shaped domain.

$$f_x(x,y) = -2\mu\pi^3 \cos(\pi y)\sin(\pi y)(2\cos(2\pi x) - 1),$$
$$f_y(x,y) = 2\mu\pi^3 \cos(\pi x)\sin(\pi x)(2\cos(2\pi y) - 1),$$

and depends only on the Lamé parameter μ and not on the critical Lamé parameter λ. The corresponding displacement solution is given as

$$u_x(x,y) = \pi\cos(\pi y)\sin^2(\pi x)\sin(\pi y),$$
$$u_y(x,y) = -\pi\cos(\pi x)\sin(\pi x)\sin^2(\pi y).$$

Notice that for the displacement solution it holds $\mathrm{div}(u) \equiv 0$. The experiments of Fig. 3.1 verify the theoretical findings of [7] and [18]. Since the convergence graphs for $\nu = 0.3$, 0.49 and 0.4999 are very close or even cover each other, these results demonstrate empirically the locking-free property of the methods, i.e., the robustness for ν tending to 1/2. Moreover, for this convex example with smooth solution, uniform refinement leads to optimal order of convergence. Fig. 3.2 shows that P_1,P_2 and P_3 lead to suboptimal convergence rates for coarser meshes because of the locking effect. However since locking is a pre-asymptotic phenomenon, the graphs show optimal convergence rates for larger number of degrees of freedom. It can be observed that all other first order methods lead to smaller errors with optimal convergence without pre-asymptotic ranges and thus no locking phenomena. Among those, the AW15 MFEM shows the smallest errors. Note that the KS non-conforming FEM and the S15 and PEERS MFEM lead to significantly larger errors than the AW21 or AW15 MFEM. The locking of the P_2 element leads to the fact that the AW24 and S27 MFEM, which are of the same order of convergence, show similarly better results. The AW30 MFEM leads to smaller errors than the P_3 FEM. Since the fourth-order P_4 FEM is locking free, it shows faster convergence rates and smaller errors than the third-order AW30 MFEM.

3.2. Cook's membrane problem

The Cook's membrane benchmark problem considers the model problem (1.1) with Ω depicted in Fig. 3.3. The domain describes a tapered panel which is clamped on the left side and subject to a surface load in vertical direction on the right side. The interior load is zero, $f \equiv 0$. For $(x,y) \in \Gamma_N$, the surface load is given by $g(x,y) = (0,1)$ if $x = 48$ and $g(x,y) = 0$ elsewhere. Since the plate is clamped, $u_D \equiv 0$ on Γ_D. This benchmark problem is a standard test for bending dominated response. In the experiments, the elasticity modulus is $E = 10^5$ and the Poisson ratio $\nu = 0.499$. Fig. 3.4 shows the displacement solution magnified by a factor of $2 \cdot 10^3$ and the modulus of the deviatoric part $|\mathrm{dev}(\sigma)|$ pictured as grey scales for the AW15 element. The unknown solution is singular because of the chosen mixed boundary conditions. Therefore, the error is approximated by the difference between the discrete solution and a fine grid approximation. The fine grid approximation is computed on a uniform refinement of the grid for the last level. For the P_k, $k = 1,\ldots,4$, FEM, the fine grid solution is computed additionally with one order higher polynomials. Fig. 3.5 shows the convergence history for uniform refined meshes. The first observation is that the convergence rate is suboptimal for all FEM due to the regularity constraints. Remark that it is unclear how to use graded meshes to improve the convergence rates. Hence, adaptive refinement strategies have to be investigated. For this benchmark example it turns out to be a crucial point for the KS FEM, that the first component is non-conforming. Choosing the second component to be non-conforming and hence the first continuous, results in singular discrete algebraic systems. This could be avoided by bisection the upper right triangle such that not all nodes of the resulting triangles lay on the Neumann boundary. The locking-effect is visible only for the linear P_1 FEM because of the dominating regularity constraints. The P_4 FEM shows the best results. The P_3 or P_2 FEM lead to similar errors as the MFEM or the KS FEM. Among the

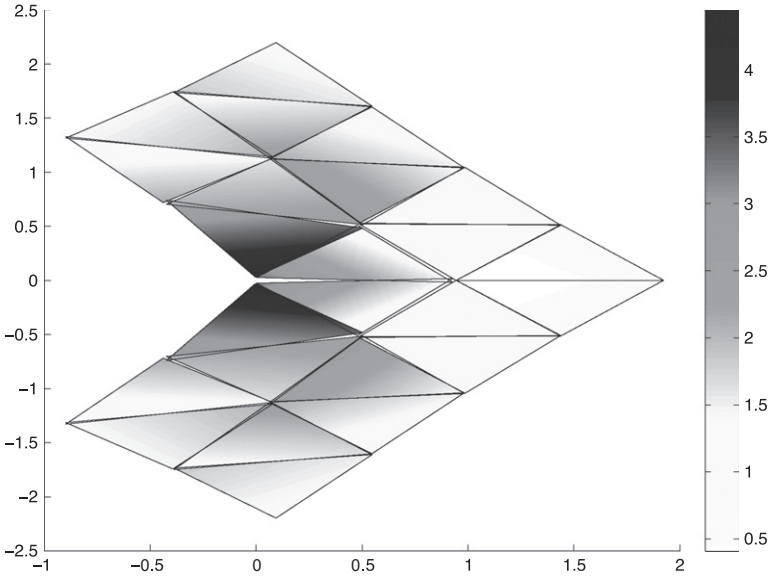

Fig. 3.10. Solution of the L-shaped benchmark.

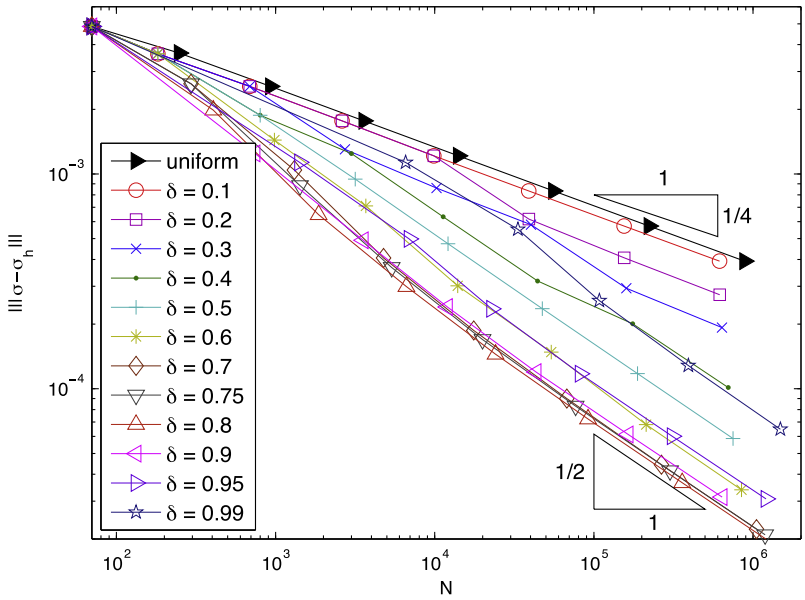

Fig. 3.11. Energy errors $|||\sigma - \sigma_h|||$ for different grading parameters δ for the low-order AW15 MFEM for the L-shaped example with Poisson ratio $\nu = 0.499$.

MFEM and the KS FEM, the AW15 shows the best results while PEERS and on the finest grid also KS show the largest error.

3.3. Circular inclusion

As a third example, consider a rigid circular inclusion in an infinite plate for the domain Ω as shown in Fig. 3.6. The exact solution [17] to the model problem (1.1) in polar coordinates (r, ϕ) reads

$$u_r = \frac{1}{8\mu r}\left((\kappa-1)r^2 + 2\gamma a^2 + \left(2r^2 - \frac{2(\kappa+1)a^2}{\kappa} + \frac{2a^4}{\kappa r^2}\right)\cos(2\phi)\right),$$

$$u_\phi = -\frac{1}{8\mu r}\left(2r^2 - \frac{2(\kappa-1)a^2}{\kappa} - \frac{2a^4}{\kappa r^2}\right)\sin(2\phi),$$

where $\kappa = 3 - 4\nu$, $\gamma = 2\nu - 1$, $a = 1/4$ and μ is the Lamé parameter determined by $E = 10^5$ and the Poisson ratio $\nu = 0.499$. Fig. 3.7 shows the displacement solution magnified by a factor of $5 \cdot 10^4$ and the modulus of the deviatoric part $|\mathrm{dev}(\sigma)|$ as grey scales for the AW21 element. The numerical comparison in Fig. 3.8 shows optimal convergence rates for the first-order methods while suboptimal convergence rates for the higher-order schemes. This is caused by the linear approximation of the boundary at the circular inclusion which is not sufficiently accurate for the higher-order methods. Therefore, for problems with curved boundary, parametric elements have to be used in order to get optimal convergence rates. Note that the implementation of parametric elements for the MFEM is somewhat more involved than the presented simplified implementation. The experiments illustrate that P_1 and P_2 show locking while for P_3 and P_4 the constraint of the boundary approximation dominates the error. For the first-order stable methods, the AW15 finite element exhibits the best results. The overall smallest error shows the AW24 MFEM.

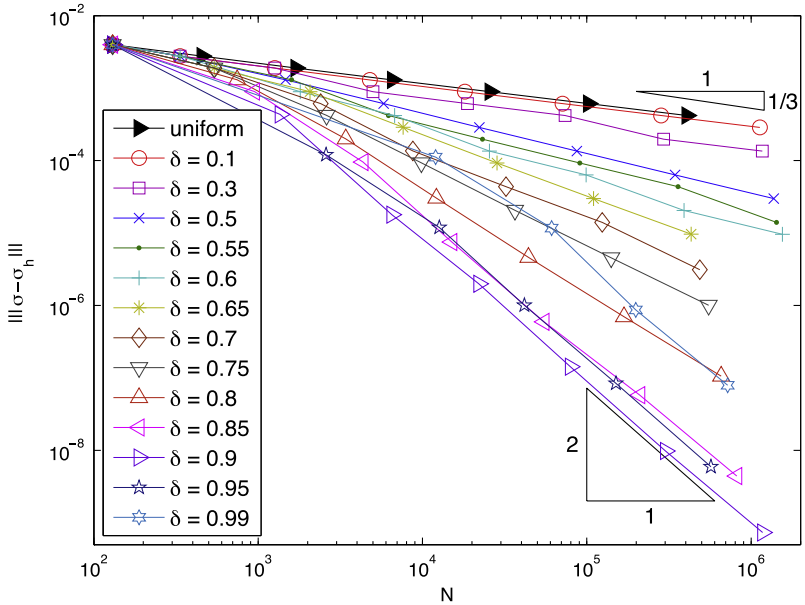

Fig. 3.12. Energy errors $|||\sigma - \sigma_h|||$ for different grading parameters δ for the high-order AW30 MFEM for the L-shaped example with Poisson ratio $\nu = 0.499$.

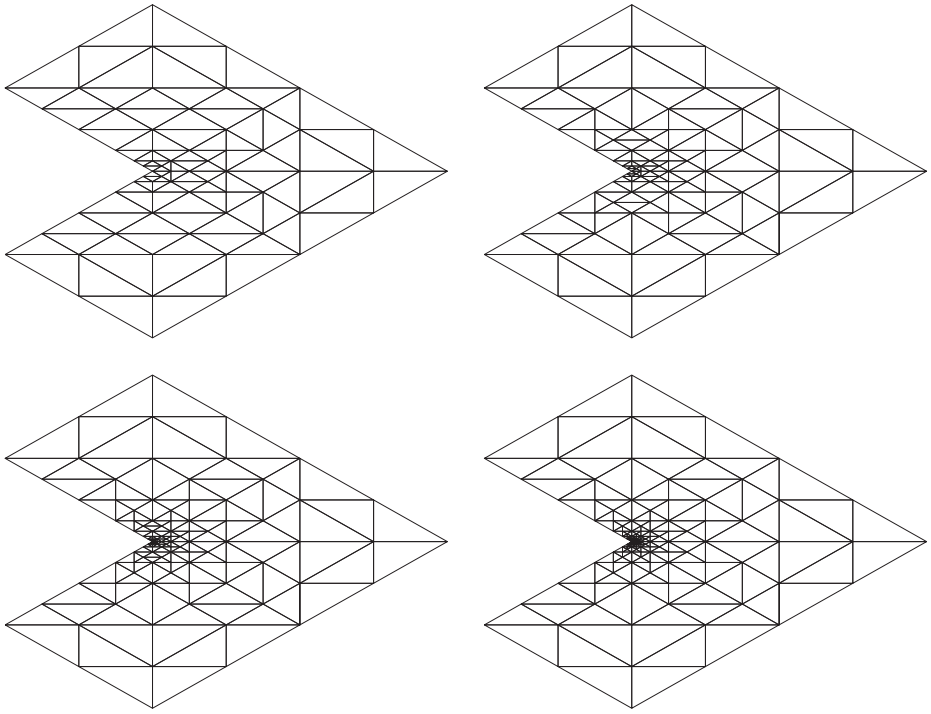

Fig. 3.13. Graded meshes for $\delta = 0.6, 0.7, 0.8, 0.9$ (top left to bottom right) for global mesh-size 1/4.

3.4. L-shaped benchmark

The last example considers the model problem (1.1) where Ω is a rotated L-shaped domain as depicted in Fig. 3.9. The exact singular solution in radial components is given by

$$u_r(r,\phi) = \frac{r^\alpha}{2\mu}(-(\alpha+1)\cos((\alpha+1)\phi) + (C_2-\alpha-1)C_1\cos((\alpha-1)\phi)),$$
$$u_\phi(r,\phi) = \frac{r^\alpha}{2\mu}((\alpha+1)\sin((\alpha+1)\phi) + (C_2+\alpha-1)C_1\sin((\alpha-1)\phi)),$$

in the polar coordinate system (r,ϕ) with $-\pi < \phi \leqslant \pi$. The constants read $C_1 := -\cos((\alpha+1)\omega)/\cos((\alpha-1)\omega)$ and $C_2 := 2(\lambda+2\mu)/(\lambda+\mu)$, where $\alpha \approx 0.544483736782$ is the positive solution of $\alpha\sin(2\omega) + \sin(2\omega\alpha) = 0$ for $\omega = 3\pi/4$ and with Lamé parameter λ, μ. Here, the volume force is zero, $f \equiv 0$, and the Dirichlet boundary conditions are computed according to the exact solution. As in the previous examples, the elastic modulus is set to $E = 10^5$ and the Poisson ratio to $\nu = 0.499$. Fig. 3.10 shows the displacement solution magnified by a factor of $5 \cdot 10^3$ and the modulus of the deviatoric part $|\mathrm{dev}(\sigma)|$ as grey scales for the S15 element. In this example, the re-entrant corner leads to singular solutions which results in slower convergence for uniform meshes as shown in Figs. 3.11 and 3.12 for the AW15 and AW30 MFEM. Therefore, local mesh refinement is needed for

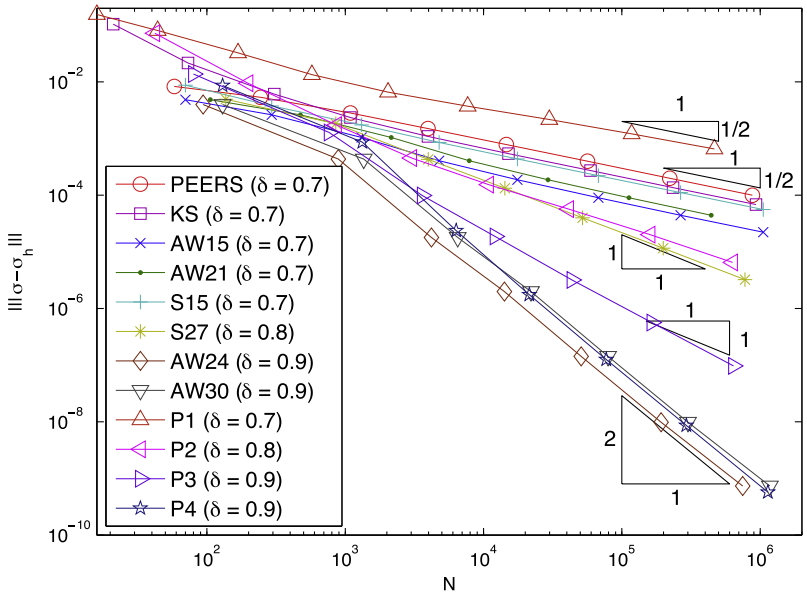

Fig. 3.14. Survey of the energy errors $|||\sigma - \sigma_h|||$ for the L-shaped example with Poisson ratio $\nu = 0.499$ on graded meshes.

optimal convergence rates. It is known that β-graded meshes can lead to better convergence rates but suffer from small angles. Therefore, the algorithm GRADMESH of [13] in combination with the red–green–blue refinement strategy [10] is used to create meshes which are more refined towards the re-entrant corner while preserving the mesh quality. Figs. 3.11 and 3.12 show the results of some experiments to determine the best grading parameter $0 < \delta < 1$ for the first-order AW15 and the third-order AW30 MFEM. For the first-order methods, a grading parameter $\delta = 0.7$ is already sufficient while for the higher-order schemes only a larger value of $\delta = 0.9$ leads to optimal convergence rates. It is observed that higher grading parameters lead to larger energy errors while lower values lead to suboptimal convergence rates. Since the right choice of the grading parameter is not known a priori, other local mesh refinement strategies such as adaptive finite element methods have to be investigated. Note that the large grading parameter $\delta = 0.9$ for the high-order methods leads to strong refinement towards the origin, c.f. Fig. 3.13. The numerical experiments of Fig. 3.14 show that the locking effect reduces the convergence rates for P_k, $k = 1, 2, 3$, and that P_4 is locking-free. Among the first-order methods, the AW15 finite element shows the best results with significantly smaller errors than for PEERS. It is remarkable that the AW30 and the AW24 MFEM exhibits some superconvergence rates of $\mathcal{O}(N^{-2})$. This is in agreement of the conjecture in [13]. Hence, the errors of the AW30 and the AW24 MFEM are similar as for the one order higher P_4 FEM.

4. Conclusions

(i) The numerical experiments verify the theoretical convergence rates and robustness for $\nu \to 1/2$ for the symmetric mixed finite element methods AW30, AW24, AW21, AW15, S15 and S27 as well as for PEERS and the KS-nonconforming and the P_4-conforming FEM.

(ii) We presented a short and simple way for implementing the rather complicated mixed schemes AW21, AW15, S15 and S27.

(iii) The numerical examples confirm that P_4 is robust, while P_k, $k = 1, 2, 3$, shows locking.

(iv) Among the first-order methods P_1, PEERS, KS, AW21, AW15 and S15, the AW15 MFEM shows the best results overall.

(v) Among the second-order methods P_2, AW24 and S27, the AW24 MFEM shows the best results overall. Note that for the first two examples the S27 MFEM shows similar results but larger errors for the last two.

(vi) Among the third-order methods P_3 and AW30, the locking-free AW30 MFEM shows the better results.

(vii) The comparison of conforming FEM and the MFEM under consideration shows that only the robust version P_4 is competitive and performs best. However, the comparison of the fourth-order scheme with some third-order method clearly shows superiority of the higher-order scheme provided the exact solution is sufficiently smooth.

(viii) The experiments for the L-shaped domain illustrate that uniform refinement results in suboptimal convergence rates while graded meshes recover optimal rates. The experiments show that some too small grading parameters lead to suboptimal convergence rates while higher values result in errors of several orders of magnitude in accuracy. Since the optimal grading parameter is, in general, not known a priori, adaptive refinement strategies have to be investigated.

(ix) The experiments for the L-shaped domain leads to the conjecture that for $f \equiv 0$ the AW30 and AW24 exhibit some superconvergence phenomenon of order $\mathcal{O}(N^{-2})$. This is in agreement with the conjecture of [13]. These results of the AW30 and AW24 MFEM can compete with those of the one order higher P_4 displacements solution. Surprisingly, the S15 and S27 MFEM do not show such properties.

Acknowledgements

The authors thank one anonymous reviewer for several comments which improved the discussion of our results. In particular, he pointed us to several recent methods which could be considered in a future review. The work of the authors was supported by the German Research Foundation (DFG) in the Research Center Matheon. The work of the first author was partly supported by the World Class University (WCU) program through the National Research Foundation of Korea (NRF) funded by the Ministry of Education, Science and Technology R31-2008-000-10049-0. The third author was also supported by the graduate school BMS. The paper was finished while the authors enjoyed the kind hospitality of the Departement CSE of Yonsei University.

References

[1] D.N. Arnold, G. Awanou, R. Winther, Finite elements for symmetric tensors in three dimensions, Math. Comput. 77 (263) (2008) 1229–1251.
[2] D.N. Arnold, F. Brezzi, J. Douglas, PEERS: a new mixed finite element for plane elasticity, Jpn. J. Appl. Math. 1 (1984) 347–367.
[3] D.N. Arnold, R.S. Falk, R. Winther, Mixed finite element methods for linear elasticity with weakly imposed symmetry, Math. Comput. 76 (260) (2007) 1699–1723 (electronic).
[4] D.N. Arnold, R.S. Falk, R. Winther, Geometric decompositions and local bases for spaces of finite element differential forms, Comput. Methods Appl. Mech. Engrg. 198 (21–26) (2009) 1660–1672.
[5] D.N. Arnold, R. Winther, Mixed finite elements for elasticity, Numer. Math. 92 (3) (2002) 401–419.
[6] D.N. Arnold, R. Winther, Mixed finite elements for elasticity in the stress–displacement formulation, Current Trends in Scientific Computing (Xi'an, 2002), Contemp. Math., vol. 329, Amer. Math. Soc., Providence, RI, 2003, pp. 33–42.
[7] D.N. Arnold, R. Winther, Nonconforming mixed elements for elasticity, Math. Models Methods Appl. Sci. 13 (3) (2003) 295–307 (Dedicated to Jim Douglas, Jr. on the occasion of his 75th birthday).
[8] F. Brezzi, M. Fortin, Mixed and hybrid finite element methods, Springer Series in Computational Mathematics, vol. 15, Springer-Verlag, New York, 1991.
[9] I. Babuška, M. Suri, Locking effects in the finite element approximation of elasticity problems, Numer. Math. 62 (4) (1992) 439–463.
[10] C. Carstensen, An adaptive mesh-refining algorithm allowing for an H^1 stable L^2 projection onto Courant finite element spaces, Constr. Approx. 20 (4) (2004) 549–564.
[11] C. Carstensen, G. Dolzmann, S.A. Funken, D.S. Helm, Locking-free mixed finite element methods in linear elasticity, Comput. Methods Appl. Mech. Engrg. 190 (2000) 1701–1781.
[12] B. Cockburn, J. Gopalakrishnan, J. Guzmán, A new elasticity element made for enforcing weak stress symmetry, Math. Comput. 79 (271) (2010) 1331–1349.
[13] C. Carstensen, D. Günther, J. Reininghaus, J. Thiele, The Arnold–Winther mixed FEM in linear elasticity. Part I: Implementation and numerical verification, Comput. Methods Appl. Mech. Engrg. 197 (2008) 3014–3023.
[14] J. Gopalakrishnan, J. Guzmán, A second elasticity element using the matrix bubble, IMA J. Numer. Anal., in press.
[15] J. Gopalakrishnan, J. Guzmán, Symmetric non-conforming mixed finite elements for linear elasticity, SIAM J. Numer. Anal., in press.
[16] J. Guzmán, A unified analysis of several mixed methods for elasticity with weak stress symmetry, J. Sci. Comput. 44 (2) (2010) 156–169.
[17] R. Kouhia, R. Stenberg, A linear nonconforming finite element method for nearly incompressible elasticity and Stokes flow, Comput. Methods Appl. Mech. Engrg. 124 (3) (1995) 195–212.
[18] J. Schöberl, A. Sinwel, Tangential-Displacement and Normal–normal-stress Continuous Mixed Finite Elements for Elasticity, Tech. Report, RICAM Report 2007-10, 2007.
[19] R. Stenberg, A family of mixed finite elements for the elasticity problem, Numer. Math. 53 (1988) 513–538.